Inorganic Chemistry

pubs.acs.org/IC Article

Bioinspired Nickel Complexes Supported by an Iron Metalloligand

Jacob R. Prat, Carlo A. Gaggioli, Ryan C. Cammarota, Eckhard Bill, Laura Gagliardi, and Connie C. Lu*



Cite This: https://dx.doi.org/10.1021/acs.inorgchem.0c02041



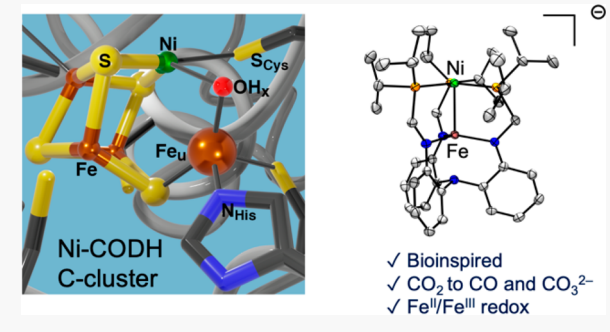
ACCESS I

III Metrics & More

Article Recommendations

Supporting Information

ABSTRACT: Nature utilizes multimetallic sites in metalloenzymes to enable multielectron chemical transformations at ambient conditions and low overpotentials. One such example of multimetallic cooperativity can be found in the C-cluster of Ni–carbon monoxide dehydrogenase (CODH), which interconverts CO and CO₂. Toward a potential functional model of the C-cluster, a family of Ni–Fe bimetallic complexes was synthesized that contain direct metal—metal bonding interactions. The complexes were characterized by X-ray crystallography, various spectroscopies (NMR, EPR, UV—vis, Mössbauer), and theoretical calculations. The Ni–Fe bimetallic system has a reversible Fe(III)/Fe(II) redox couple at -2.10 V (vs Fc⁺/Fc). The Fe-based "redox switch" can turn on CO₂ reactivity at the Ni(0) center by



leveraging the Ni \rightarrow Fe dative interaction to attenuate the Ni(0) electron density. The reduced Ni(0)Fe(II) species mediated the formal two-electron reduction of CO₂ to CO, providing a Ni–CO adduct and CO₃²⁻ as products. During the reaction, an intermediate was observed that is proposed to be a Ni–CO₂ species.

INTRODUCTION

Record high levels of atmospheric CO_2 and its detrimental impact on society motivate the development of energy-efficient processes that "fix" CO_2 into industrially useful feedstocks. ^{1–5} Arguably, the most industrially relevant C1 feedstock is carbon monoxide, with its prominent roles in Fischer—Tropsch processes and carbonylation chemistry. ⁶ In nature, CO dehydrogenases (CODHs) are highly active enzymes that use protons and electrons to interconvert CO_2 and $CO: CO + H_2O \rightleftharpoons CO_2 + 2H^+ + 2e^-$. Among CODHs, the Ni-based enzymes employ a common active site, the C-cluster, to effect this transformation. ⁷ Notably, when applied electrocatalytically, the reduction of CO_2 occurs with nearly no overpotential. ⁸

The C-cluster features a distorted NiFe₃S₄-cubane (Figure 1) that is coordinated via sulfide to an external iron site denoted as the unique iron (Fe_u). Several crystal structures of various intermediates have provided key insight into the exact binding sites for both CO and CO₂ and thereby the mechanism for their interconversion. It is believed to be the redox-active site, while Fe_u plays a supporting role in stabilizing the H₂O/OH and in assisting Ni in the cooperative binding of CO₂. Despite numerous crystallographic and spectroscopic studies, the electronic structure of the C-cluster remains elusive. Biomimetic complexes with similar cubane motifs have been synthesized, but these models do not fully mimic the position or the role of Fe_u. From the standpoint of CO₂ reactivity, only one Ni–Fe biomimetic complex has been reported that is capable of binding CO₂ to both Ni and Fe, as shown in Figure 1 (top). Excitingly, C–O

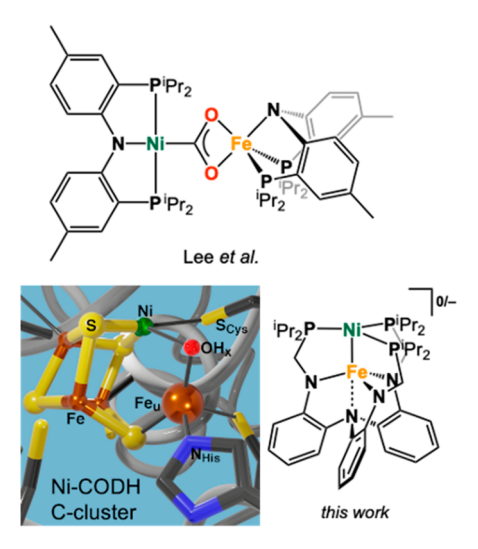


Figure 1. A zoom of the C-cluster active site in Ni-CODH and heterobimetallic NiFe model complexes.

cleavage ensued upon the addition of 2 equiv of HBF₄·Et₂O to generate a Ni carbonyl product. We note that the reactive

Received: July 9, 2020

species in this example consisted of separate mononuclear Ni and Fe precursors, as opposed to a multimetallic species that would more closely resemble the C-cluster.

To address the lack of Ni–CODH C-cluster models that are reactive toward CO₂ and feature both an active Ni center and a proximal Fe site, we set out to prepare a Ni–Fe heterobimetallic system supported by the "double-decker" ligand shown in Figure 1. Herein, we describe a redox pair of Ni–Fe complexes and their CO adducts, which were characterized by X-ray crystallography, various spectroscopies (NMR, EPR, UV–vis, Mössbauer), and theoretical calculations. In particular, the reduced Ni–Fe species allows for the observation of a presumed CO₂-bound species, a key intermediate in the overall process where CO₂ is reductively cleaved to form carbonate and a Ni-bound carbonyl adduct.

■ RESULTS AND DISCUSSION

Synthesis of Ni-Fe Bimetallic Compounds. The typical synthesis of heterobimetallic complexes bearing the doubledecker ligand, $(N(o-(NCH_2P^iPr_2)C_6H_4)_3)^{3-}$ (abbreviated as L³⁻), begins with a salt-metathesis reaction of MCl₃ and L³⁻ to afford the neutral metalloligand ML. However, attempts to prepare FeL in this manner instead formed the diiron species ClFe₂L as the major product.²² To circumvent this issue, a synthetic approach was adopted where the deprotonated ligand Li₃·L was first metalated with Ni(COD)₂ (COD = 1,5cyclooctadiene) to afford Ni(Li₃·L) in situ.²³ With the phosphines precoordinated to Ni in Ni(Li₃·L), the installation of the Fe center into the triamidoamine pocket using FeCl₃(THF)₂ proceeded cleanly, and the burgundy-colored heterobimetallic complex NiFeL (1) was isolated in 90% yield. The ¹H NMR spectrum of 1 in C₆D₆ displays six broad paramagnetically shifted peaks ranging from -55 to 88 ppm. The number of NMR peaks observed is consistent with fast interconversion of the two C₃-symmetric propeller isomers of 1 on the NMR time scale. Complex 1 is soluble in THF and aromatic solvents, is sparingly soluble in Et2O, and is insoluble in hexanes.

As shown in Scheme 1, the chemical reduction of 1 was effected using KC₈ in THF to produce a deep-red solution. The crude ¹H NMR spectrum showed six broad signals ranging from -21 to 103 ppm. Single crystals were grown from a hexane-layered THF solution at −25 °C, and an X-ray diffraction study revealed the product to be K(THF)3. NiFeL $(K-2)^{24}$ where the K⁺ ion is intercalated between two arene rings of the ligand backbone (vide infra). Correspondingly, the ¹H NMR spectrum of **K-2** displays nine sharp signals from 100 to -21 ppm. To replace K+ with a noninteracting cation, we employed the phosphazenium cation, [P(NMeCy)₄]⁺ (abbreviated as $[P_1]^+$), that was pioneered by Schwesinger and coworkers. The addition of $[P_1][BF_4]$ to the reaction of 1 and KC₈, followed by extraction into PhF, provided $[P(NMeCy)_4][NiFeL]$ ($[P_1]2$), which can be further purified by crystallization. Layering a THF solution of $[P_1]2$ with hexane resulted in black-colored needles in 65% yield. Both K-2 and [P₁]2 are sparingly soluble in Et₂O and readily soluble in THF and the fluoroarene solvents PhF, o-F₂C₆H₄, and PhCF₃.

Because carbonyl ligands are a useful reporter of metal-based electron density and CO is a pertinent substrate for Ni—CODH enzymes, the carbonyl adducts of 1 and 2 were targeted (Scheme 1). The addition of CO (1 atm) to a burgundy solution of 1 resulted in the clean production of forest green (CO)NiFeL (1-CO). In contrast, the carbonyl

Scheme 1. Synthesis of the Ni-Fe Bimetallic Compounds, K-2, [P₁]2, 1-CO, [P₁]2-CO, and [Li]2-CO, Starting from 1

adducts of the isostructural NiGaL and NiAlL complexes cannot be prepared via CO addition to the NiML precursor due to the formation of a complex mixture of species.²⁸ Complex 1-CO is remarkably soluble and even dissolves in hexanes. The addition of 1 equiv of LiHBEt3 to 1-CO generated yellow-orange $Li(THF)_4[(CO)NiFeL]([Li]2-CO)$, which was isolated in moderate crystalline yield (50%) from a THF solution layered with hexanes. Complex [Li]2-CO is soluble in THF, Et₂O, and the fluoroarene solvents PhF, o- $F_2C_6H_4$, and PhCF₃. Of note, the addition of 1 equiv of CO to a THF- d_8 solution of $[P_1]2$ generates $[P_1]2$ -CO (based on NMR), indicating another route to the reduced carbonyl complex. The CO stretch of 1954 cm⁻¹ for 1-CO (in THF) indicates moderate CO activation (cf. $\nu_{\rm CO}$ = 2143 cm⁻¹ for free CO)31 and is on par with that reported for (CO)Ni⁰(P-(OMe)₃)₃ (1952 cm⁻¹) and the isostructural (CO)NiAlL complex (1953 cm⁻¹). ^{28,32} As expected, the reduced species, [Li]2-CO, displays a lower stretching frequency of 1930 cm⁻¹ (THF, $\Delta = -24 \text{ cm}^{-1}$).

Electrochemistry of 1 and 1-CO. Cyclic voltammograms of 1 and 1-CO (0.82 mM sample, 0.1 M ["Bu₄N]PF₆/THF, 100 mV/s) showed a reversible reduction event at -2.10 V ($\Delta E_p = 184$ mV, $i_{\rm pc}/i_{\rm pa} = 1.07$) and -1.80 V ($\Delta E_p = 92$ mV, $i_{\rm pc}/i_{\rm pa} = 1.05$) versus Fc⁺/Fc, respectively (Figure 2). Additionally, a reversible oxidation process was observed at -0.37 V ($\Delta E_p = 190$ mV, $i_{\rm pc}/i_{\rm pa} = 0.92$) for 1 and at -0.20 V ($\Delta E_p = 95$ mV, $i_{\rm pc}/i_{\rm pa} = 0.94$) for 1-CO.

In general, the redox potentials for 1-CO are more positive than those for 1, which is consistent with CO being a good π -acid. Because CO withdraws electron density from the Ni–Fe core, 1-CO is both easier to reduce and harder to oxidize compared to 1. Of note, the reduction potential of 1 is milder than any of those recorded for the related Ni-group 13 compounds, NiML: -2.82 V (M = Al), -2.48 V (Ga), and -2.34 V (In). Moreover, the oxidation of 1 occurs at a more positive potential than that for NiAlL (-0.74 V) and

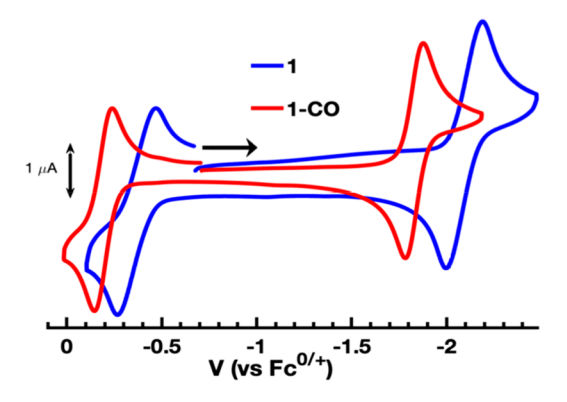


Figure 2. Cyclic voltammograms of 1 (blue) and 1-CO (red). Conditions: 0.82 mM complex and 0.1 M $[N^nBu_4]PF_6$ in THF at 100 mV/s scan rate (referenced versus Fc^+/Fc redox potential).

NiGaL (-0.57 V), while being close to that for $(N_2) NiInL$ (-0.36 V). 28,30,33

X-ray Crystallography. The solid-state structures of the Ni-Fe complexes were elucidated by single-crystal X-ray diffraction. The structures are depicted in Figure 3, and the relevant structural parameters are listed in Table 1. At 2.3168(4) Å, 1 contains the shortest reported Ni-Fe bond length to date. Previously, the shortest Ni-Fe bond length of 2.368(1) Å was reported for CpNi(η^2 -PrCCH)Fe₂(CO)₆. The formal shortness ratio (FSR), 35 or the ratio of the metal metal bond length to the sum of the metals' single-bond metallic radii, 36 is 0.93, which is suggestive of some multiplebond character (FSR < 1). Upon one-electron reduction of 1 to K-2 or $[P_1]$ 2, the Ni-Fe bond length increases substantially to 2.482(1) Å (FSR 0.99) and 2.4896(4)/2.5135(3) Å (FSR 1.00/1.01), respectively. The most notable difference between K-2 and $[P_1]$ 2 is the distortion from trigonal symmetry at the Fe site in the former because of the potassium ion interacting with the aryl ring and the N_{eq} -C(aryl) bond of the ligand.²

The addition of an apical carbonyl ligand in 1-CO causes a similar elongation of the Ni-Fe bond to 2.5183(4) Å (FSR 1.01). Moreover, the Ni center in 1-CO resides further above the triphosphine plane by 0.2962(2) Å compared to 0.0006(5) Å in 1.²⁸ In this set, [Li]2-CO, the carbonyl adduct of the reduced Ni-Fe core, has the longest intermetal distance of 2.7321(5) Å. The FSR value of 1.09 is suggestive of either noninteracting or weakly interacting metals. The C-O distances of 1.150(2) and 1.159(3) Å in 1-CO and [Li]2-CO, respectively, align with greater activation of CO upon reduction of the Ni–Fe unit (cf. 1.1283 Å in free CO).³¹ This trend in CO activation is also paralleled in the Ni-C bond length, which decreases from 1.788(2) Å in 1-CO to 1.755(3) Å in [Li]2-CO. The contraction of the Ni-C bond in [Li]2-CO is consistent with increased π -back-bonding from a more electron-rich Ni-Fe unit into the CO ligand.

Mössbauer Spectroscopy. ⁵⁷Fe Mössbauer spectroscopy is a useful spectroscopic tool for assigning Fe oxidation and spin states and even for understanding the bonding in a number of covalently bonded and bimetallic iron complexes. ^{22,29,37,38} For the anionic complexes, [P₁]2, K-2, and [Li]2-CO, the zero-field Mössbauer spectra at 80 K showed clear doublets (Figure 4, *left*). As listed in Table 2, the isomer shift (δ) values for [P₁]2, K-2, and [Li]2-CO are all similar, ranging from 0.71 to 0.75 mm/s, with quadrupole splitting ($|\Delta E_Q|$) values of 0.73, 1.04, and 1.05 mm/s, respectively. These Mössbauer parameters are characteristic of high-spin S = 2 Fe(II) centers.

In contrast to their reduced analogues, both 1 and 1-CO are S = 5/2 spin systems (based on Evans's method and EPR data, Figure S25) and displayed broad, ill-defined zero-field Mössbauer spectra at 80 K. Such excessive broadening can be observed for half-integer spin systems, where the Kramer doublet states, being easily prone to magnetic polarization, can engender large internal fields at the Fe center. The corresponding wide magnetic Mössbauer splittings, however,

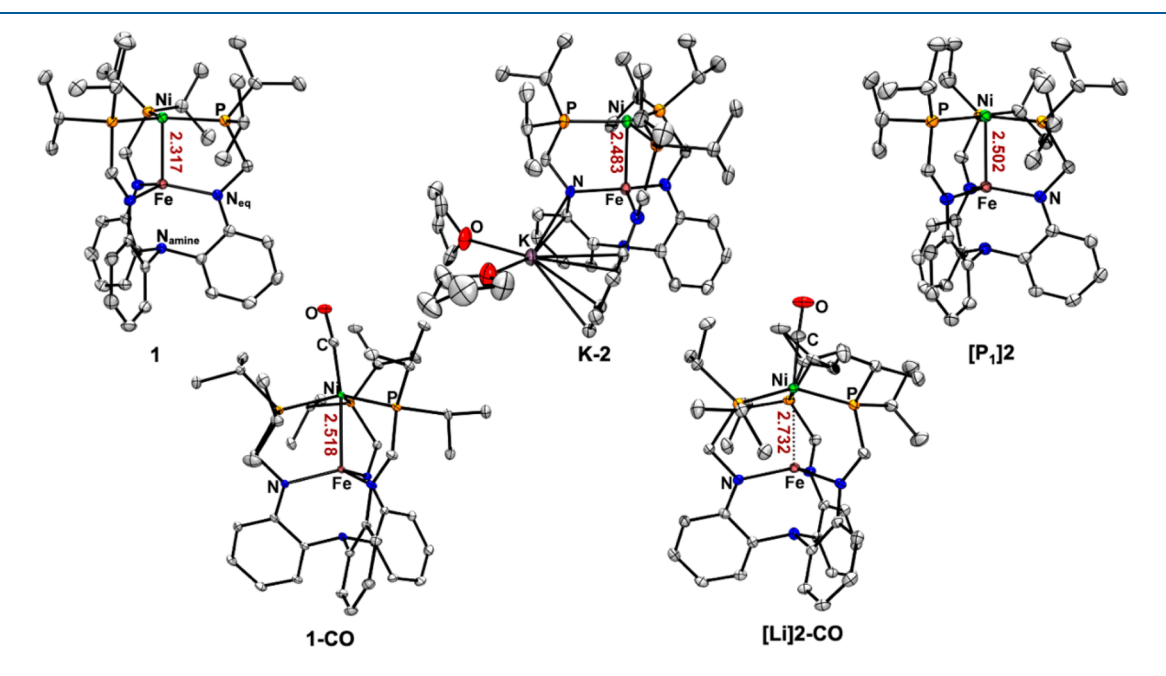


Figure 3. Solid-state structures of 1, K-2, $[P_1]2$, 1-CO, and [Li]2-CO. Thermal ellipsoids set at the 50% probability level. Hydrogen atoms, noninteracting counterions, and solvent molecules were omitted for clarity. In the case of $[P_1]2$, the average Ni–Fe bond length of two independent molecules was tabulated.

Table 1. Selected Bond Lengths (Å), Bond Angles (deg), and Other Relevant Metrics for 1, K-2, [P₁]2, 1-CO, and [Li]2-CO

	1	K-2	[P ₁]2 ^a	1-CO	[Li]2-CO
Ni–Fe	2.3168(4)	2.482(1)	2.4896(4)	2.5135(3)	2.5183(4)	2.7321(5)
FSR ^b	0.93	0.99	1.00	1.01	1.01	1.09
d-count	15	16	1	.6	15	16
Ni to P ₃ plane	0.006(3)	0.0951(9)	0.1435(4)	0.1240(4)	0.2962(2)	0.3786(4)
Ni-P	2.2258(6)	2.183(2)	2.2002(5)	2.1923(5)	2.2571(5)	2.2499(7)
	2.2307(7)	2.191(2)	2.1958(5)	2.1962(5)	2.2629(5)	2.2589(8)
	2.2434(6)	2.200(2)	2.2082(6)	2.2035(5)	2.2865(5)	2.2886(8)
P-Ni-P	118.63(2)	120.43(6)	118.79(2)	119.39(2)	115.89(2)	116.19(3)
	120.21(2)	119.51(6)	120.60(2)	119.70(2)	118.33(2)	115.79(3)
	121.16(2)	119.06(7)	119.34(2)	119.96(2)	116.89(3)	113.57(3)
Fe-N _{eq}	1.956(2)	1.997(5)	1.978(2)	1.981(2)	1.957(1)	2.000(2)
1	1.956(2)	2.017(4)	1.984(2)	1.984(2)	1.965(1)	2.000(2)
	1.957(2)	1.979(4)	1.992(2)	1.986(2)	1.966(1)	2.005(2)
Fe-N _{amine}	2.2866(16)	2.227(5)	2.198(2)	2.212(2)	2.2963(14)	2.2735(22)
N_{eq} -Fe- N_{eq}	116.17 (7)	118.65(21)	119.66(7)	119.01(6)	117.90(6)	110.62(9)
	116.98 (7)	123.95(20)	119.92(6)	116.86(6)	113.16(6)	120.29(9)
	118.67(7)	110.39(19)	114.17(7)	118.47(6)	116.31(6)	119.64(9)
C-O	N/A	N/A	N/A	N/A	1.150(2)	1.159(3)
Ni–C	N/A	N/A	N/A	N/A	1.789(2)	1.756(3)

^aTwo unique molecules in the unit cell. ^bSee text for definition.

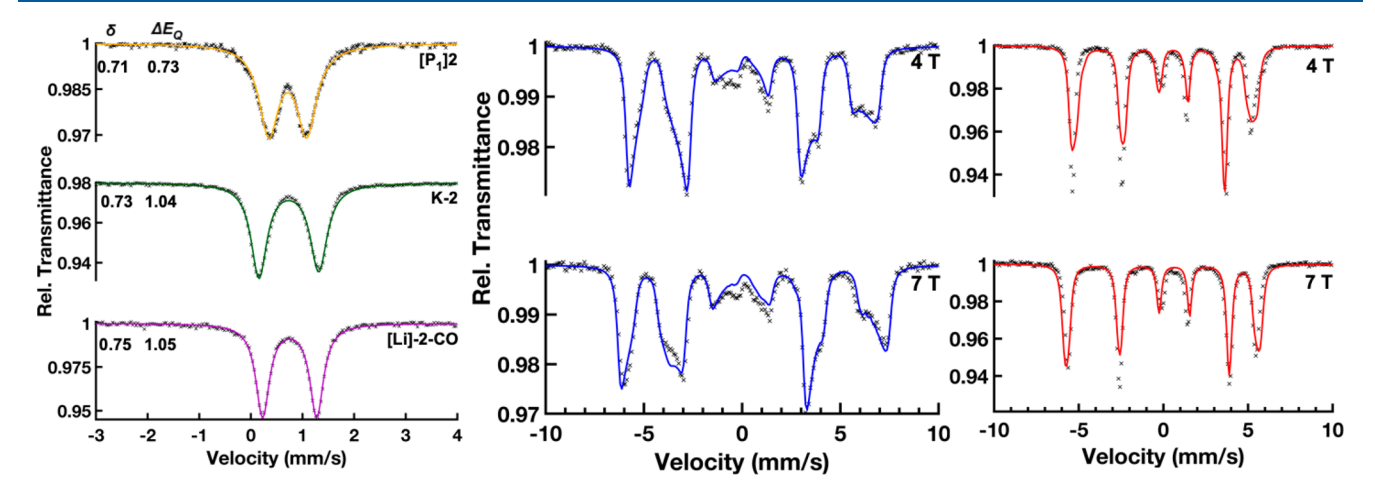


Figure 4. (*left*) The zero-field Mössbauer spectra of $[P_1]2$, K-2, and [Li]2-CO at 80 K. Magnetic Mössbauer spectra for 1 (*middle*) and 1-CO (*right*) recorded at 1.6 K with fields of 4 and 7 T applied perpendicular to the γ-rays. Experimental data are shown as black markers (×). The colored traces represent fits with Lorentzian doublets for the zero-field spectra (left) and spin-Hamiltonian simulations for others. The values obtained from parameter optimization are provided in Table 2.

Table 2. Mössbauer Parameters of 1, 1-CO, [P₁]2, K-2, and [Li]2-CO from Data Collected at Various Temperatures and Applied Fields^c

complex	$\delta \; (\text{mm/s})$	$\Delta E_Q (\text{mm/s})$	temp (K)	S	applied field (T)	$A_{zz}/g_N\mu_N$ (T)	$D \left(\mathrm{cm}^{-1} \right)$	E/D
1	0.24	+1.67 ^a	1.6	5/2	4, 7	-17.7	-0.46	0
1-CO	0.29	-0.78^{a}	1.6	5/2	4, 7	-15.0	-2.87	0.05
$[P_1]2$	0.71	0.73 ^b	25	2	0	N/A	N/A	N/A
K-2	0.73	1.04 ^b	80	2	0	N/A	N/A	N/A
[Li]2-CO	0.75	1.05 ^b	80	2	0	N/A	N/A	N/A

^aThe sign is extracted from the magnetic simulations, whereas the asymmetry parameter (η) was set to zero. ^bThese reflect the absolute value, $|\Delta E_O|$, since the sign is not determined by zero-field spectra. ^cThe g Zeeman value was set to g = 2, in accordance with EPR, Figure S25.

in weak- and zero-field measurements tend to collapse because of spin-relaxation processes, yielding a broad, unresolved coalescence pattern due to the intermediate spin-relaxation rate.

Fortunately, the paramagnetic Mössbauer spectra of 1 and 1-CO become resolved upon cooling to 1.6 K and applying external fields of 4 and 7 T. The resulting wide split six-line pattern reveals the presence of strong internal fields of more than ca. 40 T, whereas the intensity distribution of lines suggests situations with 'easy axes of magnetization', as expected for spin sextets with low-lying $m_s = \pm 5/2$ Kramers doublets. Corresponding global fits of the spectra were

Figure 5. Proposed overall reaction between 2 and CO₂ with a plausible mechanism.

performed by using spin-Hamiltonian simulations for S = 5/2to determine various parameters. The zero-field splitting parameters (D) were found to be negative, -0.46 cm^{-1} for 1 and -2.87 cm^{-1} for 1-CO, rendering the $m_s = \pm 5/2$ levels lowest in energy. (The rhombicity, E/D, for both 1 and 1-CO is zero or close to zero, which is consistent with the trigonal symmetry of these complexes and with EPR, Figure S25.) In the case of 1-CO, only the $m_s = -5/2$ level is populated at 1.6 K with 4 and 7 T applied field, and a clear single magnetic Mössbauer sextet was observed (Figure 4, right). Specifically, the combined effects of Zeeman splitting and substantial zerofield splitting of $\pm 5/2$ and $\pm 3/2$ levels by $4D \approx 12$ cm⁻¹, i.e., ca. 16 K, strongly stabilize this single m_s level. In contrast, 1, which has a substantially smaller D value $(4D/k \approx 2.6 \text{ K})$, showed a more complex pattern that derives from population of both the $m_s = -5/2$ and $m_s = -3/2$ levels (Figure 4, middle). In particular, the 'double-line' structures of the high-energy Mössbauer transitions at ca. 7 mm/s allow a sensitive determination of D. Importantly, 1 and 1-CO both have similar isomer shifts of 0.24 and 0.29 mm/s, respectively, which are significantly lower than those for the ferrous compounds and within the expected range for S = 5/2 Fe(III) centers.

For $\Delta E_{\rm Q}$, two main factors are deterministic: the principal component (V_{zz}) of the electric field gradient tensor (V_{ij}) at the iron center and the asymmetry factor, η , which is equal to $\frac{V_{xx}-V_{yy}}{V_{zz}}$. However, as the trigonal symmetry of these complexes causes vanishing η , like for E/D, the apparent quadrupole shift of the magnetic six-line Mössbauer spectra (i.e., shift of the inner four vs the outer two lines) immediately discloses ΔE_{O} , including its sign. Isostructural FeML complexes that contain Fe-M triple bonds (M = Ti, V, and Cr) are characterized by unusually large $|\Delta E_0|$ values (>4 mm/s). A detailed DFT study of the Fe-Ti series revealed that polarization of the Fe core electrons, which was attributed to the strong Fe-Ti bonding interaction, increased V_{zz} substantially.²⁹ Here, the ΔE_{O} value for 1 of 1.67 mm/s is the largest in this series and is also larger than any other Fe center in this ligand pocket (SI). Because 1 has the uniquely short Ni-Fe bond, the presence of a strong Ni \rightarrow Fe dative interaction may explain the increase in ΔE_{O} . In closing this section, we conclude the following: (1) all Fe

centers are high-spin in these Ni–Fe complexes; and (2) the one-electron reduction of both 1 and 1-CO to their anionic counterparts is completely iron-based from Fe(III) to Fe(II).

CO₂ Reductive Disproportionation. In pursuit of reactivity analogous to Ni–CODH, we tested the reactivity of the reduced Ni–Fe species with CO₂. Upon exposure of **K**-2 and 2 equiv of benzo-15-crown-5 (B-15-C-5) in THF- d_8 to 1 atm CO₂ at room temperature, a new paramagnetic species was quantitatively formed based on a clean single ¹H NMR peak at ca. 22 ppm (Figure S17). This intermediate is stable for a few hours at room temperature. Further reaction by heating at 50 °C resulted in a final mixture of **1** (major), **2**-C**0** (minor), and CO_3^{2-} . The latter was confirmed by ¹³C NMR spectroscopy using labeled ¹³CO₂ and performing a basic aqueous workup of the reaction (Figure S21). In the absence of B-15-C-5, the reaction proceeds to the same mixture of products at 40 °C, though no intermediate was detected.

Based on the product mixture, we propose that 2 mediates the reductive disproportionation of CO_2 , where $2CO_2 + 2e^- \rightarrow$ CO + CO₃²⁻, according to the stoichiometry shown in Figure 5. Since each molecule of 2 supplies one reducing equivalent, then one might expect consumption of 2 equiv of 2 and formation of 1 and 1-CO in a 1:1 ratio. However, a third molecule of 2 was further consumed to reduce 1-CO to 2-CO. In the proposed mechanism, 2 simultaneously binds and reduces CO₂ to form the Ni carboxylate species, [(CO₂)-NiFeL]-, which we tentatively assign to the observed intermediate detected electrochemically ($E_{\rm pa}$ = -1.37 V, Figure S24) and by UV-vis spectroscopy (Figure S27). Next, a one-electron reduction would produce a Ni diolate that performs a nucleophilic attack on a second molecule of CO₂. The immediate product could then cleave into 1-CO and CO₃²⁻. Finally, a second one-electron reduction would form 2-CO, alongside 2 equiv of 1. In support of this last step, combining [P₁]2 and 1-CO did produce [P₁]2-CO and 1 cleanly. To our knowledge, the standard reduction potential of $2\text{CO}_2 + 2\text{e}^- \rightarrow \text{CO} + \tilde{\text{CO}_3}^{2^-}$ in organic solvents has yet to be measured. However, using thermochemical relationships, one can calculate the potential to be -1.20 V vs Fc⁺/Fc in aqueous solution. 40 Hence, [P1]2 mediates the reductive disproportionation of CO2 with a large overpotential, not unlike many other complexes capable of CO₂ disproportionation. 41-48

If $[P_1]$ 2 was employed, where the countercation is noninteracting, the same presumed intermediate, $[(CO_2)$ -NiFeL], was immediately generated. Heating this reaction overnight at 50 °C, however, showed minimal conversion to 1 and 2-CO. This suggests that the K⁺ ions may be playing a critical role during the reaction by driving the formation of CO_3^{2-} . Indeed, performing the reaction of **K-2** in the presence of the Li⁺ source, LiAl(OR^F)₄ (where R = C(CF_3)₃), led to the instantaneous production of 1 and [Li]2-CO. A similar cation effect has been previously observed for a dianionic boranthracene CO2 reduction system and was attributed to the large enthalpic driving force of the formation of The observation of a potential CO₂ adduct is notable, as previously reported systems for reductive CO2 disproportionation typically bypass any observable adduct and proceed immediately to the metal carbonyl product or, as in the case of s- and f-block complexes, a dinuclear carbonate. 50-54 Lastly, any attempts to remove the carbonyl ligand from 1-CO or [Li]2-CO in THF- d_8 by thermolysis (50 °C, under N2 flow) or photolysis (mercury lamp, intermittent freeze-pump-thaw cycles) resulted in no reaction.

Computational Study. In order to gain insights into the electronic structure, multireference calculations were carried out for 1, [P₁]2, 1-CO, and [Li]2-CO, omitting any countercations. Single-point energies were calculated at the experimental structures for all possible spin states using complete and restricted active-space self-consistent field (CASSCF and RASSCF) methods, followed by second-order perturbation theory (CASPT2 and RASPT2). Figure 6 shows

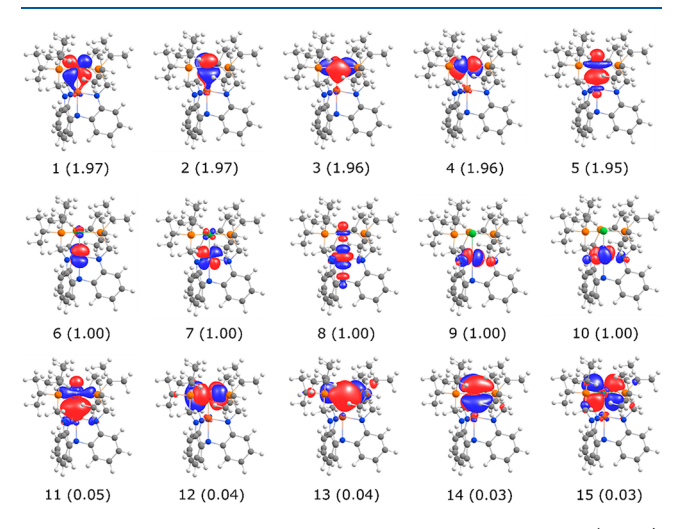


Figure 6. Natural orbitals that arise from the CASSCF(15,15) calculations for the sextet spin state for complex **1**. The orbitals are labeled 1 to 15, and the occupation numbers are shown in parentheses.

the active orbitals obtained from the CASSCF(15,15) calculation for 1, where the active space comprises 15 total valence d-electrons in 15 orbitals, which are the full sets of Ni and Fe 3d orbitals as well as the Ni 4d orbitals to account for second-shell effects. Since we expect the second-shell effects to be more pronounced for orbitals that are doubly occupied (namely, the 3d orbitals of Ni), we did not include a second shell of d orbitals for singly occupied orbitals (such as the 3d orbitals of Fe). The ground state of 1 is the sextet state (S = 5/2), which is also the highest possible spin (Table S4).

The occupation numbers are consistent with a Ni(0) d^{10} center and a high-spin Fe(III) center. The Hirshfeld spin densities corroborate this assignment with respective spin densities of 0.17 and 4.51 for Ni and Fe, respectively. Moreover, attempts to converge to the alternative configuration of Ni(I)Fe(II) as ground state were unfruitful. While the majority of natural orbitals corresponds to localized atomic orbitals, two orbitals, labeled 5 and 11 in Figure 6, show some degree of covalency. These orbitals show some $\sigma(\text{Ni-Fe})$ bond character, even though they are still quite localized on the Ni or Fe atom. Specifically, the $\sigma(\text{Ni-Fe})$ is 86% Ni $3d_z^2$ and 9.3% Fe $3d_z^2$ (Table 3). Based on their respective occupancies, we can determine a maximal Ni–Fe bond order of 0.48.

Table 3. Ni–Fe Bond Length (Å) and Ni and Fe Contributions to the $\sigma(\text{Ni-Fe})$ Orbital for 1, $[P_1]2$, 1-CO, and [Li]2-CO

	1	1-CO	$[P_1]2$	[Li]2-CO
Ni-Fe bond length	2.3168(4)	2.5183(4)	2.4896(4)	2.7321(5)
Fe $3d_{z^2}$ contribution (%)	9.3	8.1	2.4	1.8
Ni $3d_z^2$ contribution (%)	86.0	84.3	95.1	93.8

For the anionic complexes, the corresponding active space of (16,16) reaches the limit of computational feasibility. To reduce the computational cost, the Ni-Fe complexes were computed using RASSCF with the following active spaces: (15,15)/(5,5)/2 for 1 and 1-CO and (16,16)/(4,4)/2 for [P₁]2 and [Li]2-CO (see the Experimental Section for computational details). Using 1 as an example, the 15 valence electrons in 15 orbitals are further restricted to 5 electrons in 5 active orbitals (in the RAS2 subspace), while allowing for 2 particles (at maximum) to populate the virtual orbitals. The predicted ground state and metal spin densities from the RASSCF/PT2 calculations of 1 were the same or highly similar to those obtained from the CASSCF/PT2 study (Table S4). Across the remaining Ni-Fe complexes, the highest spin configuration was consistently predicted to be the ground spin state. Moreover, the Ni spin density remains consistently near zero, while the Fe spin density is consistent with high-spin Fe(III) in 1-CO or high-spin Fe(II) in $[P_1]$ 2 and [Li]2-CO (Tables S5-S7). These results along with the Mössbauer data reinforce the fact that the redox changes are Fe-based, via the Fe(II)/Fe(III) redox couple, while Ni remains primarily invariant as Ni(0).

The extent of localization in the $\sigma(\text{Ni-Fe})$ orbital for 1-CO (84.3% Ni $3d_z^2$, 8.1% Fe $3d_z^2$) is slightly greater than that for 1 (Table 3). The reduced analogues, [P₁]2 and [Li]2-CO, show even greater polarization with the Ni $3d_z^2$ character as high as 93 to 95%. These results suggest that the Ni–Fe covalency is greater in the oxidized Ni(0)Fe(III) species than in their reduced Ni(0)Fe(II) analogues. However, considering the strong localization of these molecular orbitals, the Ni–Fe bonding interaction is highly dative in nature with Ni \rightarrow Fe donation. Hence, a highly Lewis acidic Fe(III) acceptor could account for the short Ni–Fe bond found in 1. The ca. 0.2 Å metal—metal bond length increase upon reduction (cf. 1 to [P₁]2 and 1-CO to [Li]2-CO) can also be explained by both the decreased covalent character and the lower Lewis acidity of Fe(II) in the reduced counterparts. Lastly, the ca. 0.2 Å metal—

metal bond length increase upon CO binding would also be consistent with decreased electron density at Ni, which weakens the Ni→Fe dative interaction.

Comparison with the C-Cluster of Ni–CODH. One key aspect of Ni–CODHs is their high structural similarity across different bacteria phyla, hinting at the fundamental nature of the design principles that govern their function. The C-cluster, which mediates the interconversion of CO and CO₂ (via CO + $H_2O \rightarrow CO_2 + 2H^+ + 2e^-$), has been investigated extensively using varied spectroscopic and structural methods. While the consensus has been reached regarding its geometric structure as a distorted NiFe₃S₄-cubane with a dangling unique Fe (or Fe_u), the electronic structure remains elusive, and the specific metal oxidation states are not fully known. Hence, there is ample opportunity for developing model complexes to target the structural complexity of the C-cluster in order to better understand how the cluster works. T₁T₁T₁18,20

During the catalytic cycle, the C-cluster cycles between two redox states: $C_{\rm red1}$ and $C_{\rm red2}$, where $C_{\rm red1}$ is reduced in two single-electron steps to form $C_{\rm red2}$. More importantly, $C_{\rm red2}$ binds CO_2 , and an X-ray structure of the $C_{\rm red2}+CO_2$ state revealed the CO_2 substrate bridging between Ni and Fe_u in a Ni–C(O)–O–Fe_u linkage. 12,57 In the proposed mechanism, subsequent protonation followed by full cleavage of the C–O bond yields Ni–CO and Fe_u –OH in the $C_{\rm red1}+CO$ state. The Ni/Fe_u oxidation states in $C_{\rm red1}$ and $C_{\rm red2}$ are proposed to be Ni(II)/Fe_u(II) and Ni(O)/Fe_u(II), respectively, where the reduction is Ni-based. Moreover, Fe_u was assigned as the high-spin ferrous component that had been observed by Mössbauer spectroscopy.

In comparison to the C-cluster, the synthetic Ni-Fe complexes herein feature an overly simplified cluster comprising a Ni atom paired with a single Fe ion. Nonetheless, the reduced Ni(0)Fe(II) core in 2 shares the same oxidation/ spin states as those proposed for Ni and Fe_u in C_{red2}. Moreover, 2 binds CO₂ akin to C_{red2}. However, CO₂ binding to 2 presumably occurs solely at Ni because the ligand scaffold precludes the Fe center from readily interacting with substrates. Without the possibility to employ both Ni and Fe to activate CO₂, the cleavage of CO₂ does not ensue after CO₂ binding like in Ni-CODH. Instead, a further reduction of 2-CO₂ is needed to initiate CO₂ disproportionation to carbonate and 1-CO. Because C_{red1} and C_{red2} differ by two electrons, 1/1-CO, which only differ from 2/2-CO by a single electron, are ill-suited models for C_{red1}/C_{red1}+CO. Other key contrasts between our synthetic system and the C-cluster are that the reduction of 1 is Fe-based, rather than Ni-based for Ni-CODH, and 1-CO does not release CO, which inhibits any catalytic turnover.

Another difference in the synthetic system is the presence of direct Ni–Fe bonding, where the Ni–Fe bond lengths vary from 2.32 to 2.73 Å. By contrast, Ni–Fe bonding is not invoked in the structures of $C_{\rm red1}$ and $C_{\rm red2}$, where the Ni···Fe_u distances are 2.85 and 2.88 Å, respectively. An interesting side note is that the Fe_u site is disordered over two positions in both the structures of $C_{\rm red1}$ and $C_{\rm red2}$. The minor Fe_u position (with 30% occupancy) is even closer to Ni with potentially short Ni–Fe_u distances of 2.38 and 2.44 Å, respectively. Though this partial occupancy was explained by the authors as arising from a minor component where Ni is missing, the mobility of the Fe_u ion is clearly evident in a structure of the oxidized C-cluster. Show a sail of the system of the oxidized C-cluster.

[NiFe] hydrogenases the presence of a Ni–Fe bond in the light-induced Ni–L state was strongly supported by a joint spectroscopic and computational study. 59,60

CONCLUSIONS

Bimetallic complexes containing direct Ni-Fe bonding interactions were synthesized and characterized. The nature of their bonding is primarily dative, with a much stronger interaction between Ni⁰ and the Fe^{III} supporting ion compared to Fe^{II}. Both the poorer σ -acceptor propensity of the ferrous support as well as the overall anionic charge enable the Ni⁰Fe^{II} species 2 to reductively disproportionate CO2, in contrast to Ni⁰Fe^{III} 1. The identity of the countercation in 2 dictates the following: (1) the stability of the CO2 adduct, where noninteracting ions, such as P₁ and K(B-15-C-5)₂, lead to greater stability; and (2) the acceleration of CO₂ disproportionation by Li⁺ over K⁺, which may result from the differing driving forces for the carbonate products. Notably, the Ni⁰Fe^{II} core in 2 contains the same proposed oxidation/spin state of the reduced state of the Ni–CODH C-cluster (C_{red2}) and is, to our knowledge, only the second example of a Ni-Fe complex that mediates the cleavage of CO₂ to CO.²¹

The Ni–Fe complexes feature an accessible one-electron reduction potential that allows for switching between a Fe^{III} support and a Fe^{III} support, the latter of which is much less Lewis acidic toward Ni⁰. This facile Fe^{III}/Fe^{III} redox couple is reminiscent of redox switchable catalysts that employ a ferrocene motif. Using metal—metal bonded complexes to perform redox switchable catalysis is currently underexplored and may be a promising subsequent avenue of research. In future work, catalysts with ligands more closely matching the relevant ligand interactions in the NiFe₃S₄ C-cluster will be explored for their reactivity with CO₂, ideally benefiting from a more fluxional metal—metal interaction that can dynamically adapt to the changing electronic states during catalysis.

EXPERIMENTAL SECTION

General Considerations. Unless otherwise stated, all manipulations were performed under a N2 atmosphere in a glovebox. Celite and molecular sieves were dried at 340 °C under vacuum. Standard solvents were deoxygenated by sparging with inert gas and dried by passing through activated alumina columns of a SG Water solvent purification system. Deuterated solvents were purchased from Cambridge Isotope Laboratories, Inc., degassed via freeze-pumpthaw cycles, and stored over activated 4 Å molecular sieves. KC₈, N(o-(NHCH₂PⁱPr₂)C₆H₄)₃ (abbreviated as LH₃), and [P(NCH₃C₆H₁₁)₄]-BF₄ (abbreviated as [P₁]BF₄) were prepared according to literature methods.^{25,66,67} Benzo-15-crown-5 was purified by double recrystallization from hexanes at -78 $^{\circ}C$ and dried under vacuum. All other reagents, including 13CO2, were purchased from Sigma Aldrich or Strem Chemicals and used without further purification. Ultrahigh purity CO₂ was passed through a column of anhydrous sodium sulfate prior to use. Elemental analyses were performed by Robertson

Microlit Laboratories, Inc. (Ledgewood, NJ).

Physical Methods. ¹H and ³¹P NMR spectra were recorded on a Bruker 400 MHz spectrometer. NMR shifts were referenced to the internal solvent residual signal (for ¹H spectra) or an external H₃PO₄ reference (for ³¹P spectra). Evans's method measurements were done in triplicate according to previously outlined procedures. ⁶⁸ Perpendicular-mode X-band EPR spectra were recorded with a Bruker ESP 300 spectrometer equipped with an Oxford Instruments ESR 910 liquid-helium cryostat and an Oxford Instruments temperature controller. EPR spectra were simulated utilizing Easyspin with the pepper function (frozen solution) and refined using *esfit* until a satisfactory model was obtained. IR spectra were obtained in KBr

Table 4. Crystallographic Details for 1, K-2, [P₁]2, 1-CO, and [Li]2-CO

	1	K-2	$[P_1]2$	1-CO	[Li]2-CO
chemical formula	$C_{39}H_{60}N_4P_3FeNi$	$C_{39}H_{60}N_4P_3KNiFe \cdot (OC_4H_8)_3$	$\begin{bmatrix} C_{28}H_{56}N_4P \end{bmatrix} \ \begin{bmatrix} C_{39}H_{60}N_4P_3NiFe \end{bmatrix}$	$\begin{matrix} C_{40}H_{60}N_4OP_3NiFe \\ \cdot C_6H_{14} \end{matrix}$	$ \begin{array}{c} [\text{Li}(\text{OC}_4\text{H}_8)_4] \\ [\text{C}_{40}\text{H}_{60}\text{N}_4\text{OP}_3\text{NiFe}] \end{array}$
fw	792.38	975.68	1272.10	906.56	1114.73
cryst syst	monoclinic	monoclinic	monoclinic	monoclinic	triclinic
space group	$P2_1/n$	$P2_1/c$	$P2_1/c$	$P2_1/c$	$P\overline{1}$
a (Å)	13.5937(18)	22.0875(13)	23.1460(9)	11.8280(12)	11.2284(13)
b (Å)	13.9349(18)	14.3441(8)	32.7259(12)	16.0475(17)	12.6905(9)
c (Å)	20.817(3)	17.1129(9)	21.4025(7)	24.308(2)	20.965(3)
α (deg)	90	90	90	90	83.337(4)
β (deg)	94.340(2)	97.447(2)	100.697(1)	101.262(3)	77.277(5)
γ (deg)	90	90	90	90	89.334(4)
V (Å ³)	3932.0(9)	5376.1(5)	15930.1(10)	4525.1(8)	2894.1(5)
Z	4	4	8	4	2
$D_{\rm calcd}~({ m g~cm^{-3}})$	1.339	1.205	1.061	1.331	1.279
θ range (deg)	1.731 to 27.521	2.340 to 28.282	2.210 to 26.48	2.198 to 30.568	2.442 to 30.546
T (K)	173(2)	100(2)	125(2)	100(2)	100(2)
reflns collected	9029	13335	406948	13855	17597
unique reflns	6330	10031	39630	11019	12520
λ (Å), μ (mm ⁻¹)	0.71073, 0.6228	0.71073, 0.5797	0.71073, 0.537	0.71073, 0.6897	0.71073, 0.4938
data/restraints/ param	9029/0/445	13335/ 10 /560	39630/0/1491	13855/0/519	17597/12/674
R_1 , wR_2 $(I > 2\sigma(I))$	0.0340, 0.0673	0.0861, 0.1980	0.0401, 0.0915	0.0468, 0.1117	0.0590, 0.1444
R_1 , wR_2 (all data)	0.0554, 0.0735	0.1166, 0.2141	0.0623, 0.1034	0.0673, 0.1202	0.0930, 0.1719
CCDC numbers	2015103	2015105	2015515	2015104	2015106

pellets using a Bruker Tensor-37 FTIR spectrometer with OPUS 6.5 software. Mössbauer spectra were modeled using the program MFit written by Eckhard Bill from the Simulation Lab suite. ⁶⁹ Mössbauer data were recorded on an alternating constant-acceleration spectrometer. The minimum experimental line width was 0.24 mm/ s⁻¹ (full width at half-height). The ⁵⁷Co/Rh source (1.8 GBq) was positioned at r.t. inside the gap of the magnet system at a zero-field position. Isomer shifts are quoted relative to Fe metal at 300 K. Cyclic voltammetry was conducted using a CH Instruments 600 electrochemical analyzer. The one-cell setup utilized a glassy carbon working electrode, a Pt wire counter electrode, and an Ag wire pseudoreference electrode. Analyte solutions were prepared in 0.4 M ["Bu₄N]PF₆ in THF and referenced internally to the FeCp₂+/FeCp₂ redox couple. UV—vis spectra were collected on a Cary-300 instrument.

Synthesis of NiFe(N(o-(NCH₂P i Pr₂)C₆H₄)₃), 1. To a stirring solution of LH₃ (237 mg, 348 μ mol) in 10 mL of toluene at -78 °C was added dropwise "BuLi (2.5 M hexanes, 418 μL, 1.04 mmol). The reaction was stirred for 30 min at -78 °C and then for 3 h at room temperature before being filtered through a glass frit. The filtride was washed with pentane (3 × 6 mL) to afford Li₃L as a white solid. To a stirring suspension of Li₃L in 10 mL of toluene was added solid $Ni(COD)_2$ (95.8 mg, 348 μ mol), and the solution was stirred overnight and then filtered through a glass frit. The red filtride was washed with pentane (3 × 10 mL) and dried in vacuo to afford Li₃NiL, which was used immediately in the next step. To a stirring solution of Li₃NiL in 10 mL of THF was added dropwise a solution of FeCl₃(THF)₂ (106.7 mg, 348 μ mol) in 4 mL of THF. The reaction was stirred for 3 h, and then all volatiles were removed in vacuo. To the resulting residue was added ca. 4 mL of toluene, and then the mixture was dried in vacuo. The dark red-brown solid was then extracted into warm toluene (50 °C, 2 × 10 mL) and filtered through Celite. The filtrate was dried in vacuo, and the burgundy residue was washed with a 3:1 hexanes/ether solution, cooled to -78 °C (2 × 5 mL), and further dried in vacuo to afford 1 (242.8 mg, 88% yield). Single crystals were grown by the diffusion of pentane into a concentrated benzene solution of 1. ¹H NMR (400 MHz, C_6D_6): δ 88, 56, 21, -4.1, -42, -57. μ_{eff} (Evans) = 5.6(2) B.M. UV-vis [THF, λ_{max} (nm), ε (M⁻¹ cm⁻¹)]: 350 (12,450), 410 (9300), 550 (3750). Anal. Calcd for C₃₉H₆₀N₄P₃FeNi (%): C, 59.12; H, 7.63; N, 7.07. Found: C, 58.86; H, 7.56; N, 7.01.

Synthesis of (CO)NiFe(N(o-(NCH₂PⁱPr₂)C₆H₄)₃), 1-CO. In the glovebox was prepared in a resealable glass ampule a solution of NiFeL (43.7 mg, 55.1 μ mol, 15 mL THF). Vacuum was briefly applied to vacate the headspace of the reaction vessel. The vessel was attached to a Schlenk line where CO gas was admitted. The vessel was sealed and inverted several times to ensure proper gas mixing. The solvent was then removed *in vacuo* to give a dark green residue. The desired product was extracted into hexanes (4 × 4 mL), filtered over Celite, and dried (32.9 mg, 75% yield). ¹H NMR (400 MHz, C_6D_6): δ 75, 33, 21, 18, -51, -74. IR (KBr, cm⁻¹): 1954 (ν _{CO}). IR (THF, cm⁻¹): 1953 (ν _{CO}). UV-vis [THF, λ _{max} (nm), ε (M⁻¹ cm⁻¹)]: 350 (13,400), 475 (6200), 615 (3900). Anal. Calcd for $C_{40}H_{60}N_4P_3$ OFeNi·0.5(C_6H_{14}) (%): C_7 59.81; H, 7.82; N, 6.49. Found: C_7 59.73; H, 8.11; N, 5.92. Elemental analysis could be consistent with some partial solvent loss, though N is low.

Synthesis of [Li(THF)₄][(CO)NiFe(N(o-(NCH₂PⁱPr₂)C₆H₄)₃)], [Li]2-CO. To a stirring solution of 2 (12.1 mg, 0.0148 mmol, 10 mL THF) was added dropwise a LiHBEt₃ solution (1.0 M THF, 15 μL). Over the course of 30 min, the solution darkened to a brown color. After 12 h, the solution had turned orange. The solution was concentrated *in vacuo* to *ca*. 6 mL and then layered with hexanes. Orange/yellow needle crystals were observed after 3 d. The crystals were separated from the mother liquor and washed with hexanes (8.6 mg, 50% yield). ¹H NMR (400 MHz, THF- d_8): δ 104, 56, 25, 20, 13.4, -5.4, -15.7, -22. IR (THF, cm⁻¹): 1930 (ν_{CO}). OUV-vis [THF, λ_{max} (nm), ε (M⁻¹ cm⁻¹)]: 305 (23,500). Anal. Calcd for [LiO₄C₁₆H₃₂][C₄₀H₆₀N₄P₃OFeNi] (%): C, 60.28; H, 8.31; N, 5.02. Found: C, 57.17; H, 8.02; N, 4.97. The elemental analysis results are consistent with partial solvent loss and oxidation of the phosphines. Anal. Calcd for [LiO₃C₁₂H₂₄][C₄₀H₆₀N₄P₃O₄FeNi] (%): C, 57.17; H, 7.16; N, 5.13.

Synthesis of K(THF)₃·NiFe(N(o-(NCH₂ P^i Pr₂)C₆H₄)₃), K-2. To a 10 mL THF solution of 1 (31.6 mg, 39.9 μ mol) was added KC₈ (5.6 mg, 41.1 μ mol). The wine-red solution was stirred for 3 h and then filtered over Celite. The filtrate was concentrated in vacuo to ca. 2 mL. To this solution was added 8 mL of hexanes, and the volume was slowly reduced *in vacuo* until crystalline precipate was observed. The solution was then stored at -35 °C overnight to yield 28.5 mg of black crystals after separation from the mother liquor. The mother liquor was further concentrated to ca. 10 mL and layered with hexanes

at -35 °C to obtain more crystals (total: 38.7 mg, 95% yield). 1H NMR (400 MHz, THF- d_8): δ 101, 71, 56, 10, 16, 16, 13.5, 12.3, -20, -21. $\mu_{\rm eff}$ (Evans) = 5.13 $\mu_{\rm B}$ UV-vis [THF, $\lambda_{\rm max}$ (nm), ε (M $^{-1}$ cm $^{-1}$)]: 515 (8,500), 655 (2400). Anal. Calcd for [K(crypt-222)][NiFeC $_{39}H_{60}P_3N_4$], [K(C $_{18}N_2H_{36}O_6$)][NiFeC $_{39}H_{60}P_3N_4$] (%): C, 56.67; H, 8.01; N, 6.96. Found: C, 57.06; H, 8.25; N, 6.54.

Synthesis of $[P(NCH_3C_6H_{11})_4][NiFe(N(o-(NCH_2P^iPr_2)C_6H_4)_3)],$ $[P_1]$ 2. In a 20 mL vial, 1 (35.0 mg, 44.2 μ mol) was stirred in ca. 10 mL of THF. To this solution was added portion-wise over a 5-min period a slurry of KC₈ (7.8 mg, 57.4 µmol) in ca. 4 mL of THF. The wine-red solution was stirred for 2 h and filtered over Celite. To this solution was added ca. 3-mL THF slurry of [P₁]BF₄ (25.0 mg, 44.2 μ mol). The slurry was stirred overnight, and then the solvent was removed in vacuo. To ensure complete removal of THF, ca. 6 mL of PhF was added to the residue. The solution was stirred and then dried under vacuum. The residue was then extracted with 10 mL of PhF, and the filtrate was filtered over Celite. This solution was directly layered with ca. 10 mL of hexanes, and a crop of black needles was obtained after 2 d. Crystals were washed with hexanes, crushed into a fine powder with a spatula, and dried (36.3 mg, 65% yield). ¹H{³¹P} NMR (400 MHz, THF- $d_{\rm s}$) δ : 115, 81, 59, 20, 16, 14, 11, 2.34 (br, NCH₃) 1.7–0.59 (m, overlapped with solvent peaks, NC₆H₁₁) –2.1, -22.5, -25. ³¹P NMR (162 MHz, THF- d_8) δ : 45.3 (P₁). $\mu_{\rm eff}$ (Evans) = 4.93(6) B.M. UV-vis [THF, $\lambda_{\rm max}$ (nm), ε (M⁻¹ cm⁻¹)]: 350 (17,280), 410 (9150), 540 (4900).

X-ray Crystallography and Structure Refinement Details. A black block of 1 (0.8 \times 0.5 \times 0.5 mm), a black plate of K-2 (0.4 \times 0.2 \times 0.2 mm), a green needle of 1-CO (0.2 \times 0.2 \times 0.1 mm), a red plate of $[P_1]2$ (0.2 × 0.2 × 0.1 mm), and a yellow needle of [Li]2-CO (0.4 \times 0.2 \times 0.2 mm) were placed on the tip of a glass capillary and mounted on a Bruker APEX-2 Platform CCD diffractometer for data collection at 173(2) K (for 1) or were mounted on a 100 μ m MiTeGen microloop and placed on a Bruker PHOTON-II CMOS diffractometer for data collection at 100(2) K (for 1-CO, K-2, and [Li]2-CO) or at 125(2) K (for $[P_1]2$). The data collection was carried out using Mo K α radiation with normal parabolic mirrors. The intensities were corrected for absorption and decay with SADABS.⁷¹ Final cell constants were obtained from least-squares fits from all reflections. Crystal structure solution was done through intrinsic phasing (SHELXT-2014/5)⁷² which provided most non-hydrogen atoms. Full matrix least-squares/difference Fourier cycles were performed (using SHELXL-2016/6 and GUI ShelXle)^{73,74} to locate the remaining non-hydrogen atoms. All non-hydrogen atoms were refined with anisotropic displacement parameters. Hydrogen atoms were placed in ideal positions and refined as riding atoms with relative isotropic displacement parameters. The crystal structures of K-2 and [P₁]2 contained heavily disordered solvent molecules. The SQUEEZE function of the PLATON program was used to remove these solvent molecules from the void space.⁷⁵ The SQUEEZE function removed 213 electrons from a void-space volume of 642 Å³ in K-2 and 643 electrons from a void-space volume of 3151 Å³ in $[P_1]$ 2. These values are consistent with the presence of approximately 4 THF molecules in the unit cell of K-2 and 8 Et₂O and 8 THF molecules in the unit cell of [P₁]2. Crystallographic details are summarized in Table 4.

Computational Methods. Single-point multireference calculations were performed using the experimental geometries with the MOLCAS-8.2 package. The complete active space self-consistent field (CASSCF) and restricted active space self-consistent field (RASSCF) methods were employed, followed by second order perturbation theory (CASPT2 ^{80,81}/RASPT2 ^{79–82}) to include dynamical correlation. All-electron basis sets of atomic natural orbital type with relativistic core corrections (ANO-RCC) were used employing a triple-ζ plus polarization basis set (VTZP) for Fe and Ni, a double-ζ plus polarization basis set (VDZP) for N, P, and the CO fragment, and a minimal basis set (MB) for the peripheral C and H atoms. The two-electron integral evaluation was simplified using the Cholesky decomposition technique. As Scalar relativistic effects were included by means of the Douglas–Kroll–Hess Hamiltonian. The CASPT2/RASPT2 calculations were performed using an IPEA shift of 0.25 au

and an imaginary shift of 0.2 au. The first 70 (72) orbitals were frozen during the CASPT2/RASPT2 calculations for the complexes without (with) the CO molecule. The Hirshfeld spin populations 86 were computed using the MultiWfn package. 87

In the CASSCF calculations, an active space (AS) of n electrons in m orbitals (n,m) is chosen, and all configurations that arise from all possible excitations of the n electrons in the m orbitals are included in the wave function. In the RASSCF calculations, the active orbitals are divided into three distinct subspaces, RAS1, RAS2, and RAS3. In RAS1, the orbitals are doubly occupied, and at most n excitations from RAS1 are allowed. In RAS2, n_{ae2} electrons in n_{ao2} orbitals are included, and a full configuration interaction is performed. In RAS3, virtual orbitals are included, and at most n excitations to RAS3 are allowed. The following notation is used: RASSCF $(n_{ae}$ in $n_{ao})/(n_{ae2}$ in $n_{ao2})/n$, where n indicates the maximum number of electrons excited from RAS1 or into RAS3 (n=2) in this work), $(n_{ae}$ in $n_{ao2})$ describes the global RAS(1-3) active space, and $(n_{ae2}$ in $n_{ao2})$ describes the RAS2 space.

ASSOCIATED CONTENT

Supporting Information

The Supporting Information is available free of charge at https://pubs.acs.org/doi/10.1021/acs.inorgchem.0c02041.

CV data, NMR spectra, X-ray crystallography data, EPR spectra, UV-vis spectra, theoretical data, and Mössbauer data (PDF)

Accession Codes

CCDC 2015103–2015106 and 2015515 contain the supplementary crystallographic data for this paper. These data can be obtained free of charge via www.ccdc.cam.ac.uk/data_request/cif, or by emailing data_request@ccdc.cam.ac.uk, or by contacting The Cambridge Crystallographic Data Centre, 12 Union Road, Cambridge CB2 1EZ, UK; fax: +44 1223 336033.

AUTHOR INFORMATION

Corresponding Author

Connie C. Lu — Department of Chemistry, University of Minnesota, Minneapolis, Minnesota 55455-0431, United States; orcid.org/0000-0002-5162-9250; Email: clu@umn.edu

Authors

Jacob R. Prat — Department of Chemistry, University of Minnesota, Minneapolis, Minnesota 55455-0431, United States Carlo A. Gaggioli — Department of Chemistry and Minnesota Supercomputing Institute & Chemical Theory Center, University of Minnesota, Minneapolis, Minnesota 55455-0431, United States; orcid.org/0000-0001-9105-8731

Ryan C. Cammarota — Department of Chemistry, University of Minnesota, Minneapolis, Minnesota 55455-0431, United States Eckhard Bill — Max-Planck-Institut für Chemische Energiekonversion, 45470 Mülheim an der Ruhr, Germany; orcid.org/0000-0001-9138-3964

Laura Gagliardi — Department of Chemistry and Minnesota Supercomputing Institute & Chemical Theory Center, University of Minnesota, Minneapolis, Minnesota 55455-0431, United States; Occid.org/0000-0001-5227-1396

Complete contact information is available at: https://pubs.acs.org/10.1021/acs.inorgchem.0c02041

Notes

The authors declare no competing financial interest.

ACKNOWLEDGMENTS

The authors thank Prof. John Lipscomb for access to the EPR spectrometer, J.T. Moore and Michael Dorantes for collecting EPR spectra, Bernd Mienert and Dr. Peter Solheid for collecting the Mössbauer spectra, and Dr. Victor G. Young, Jr. for assistance with X-ray crystallography. J.R.P. was supported by the National Science Foundation (NSF) Graduate Research Fellowship Program. The synthetic work was supported by NSF (CHE-1800110). X-ray diffraction experiments were performed using a crystal diffractometer purchased through a grant from NSF (MRI-1229400) and the University of Minnesota. The computational work was supported by NSF (CHE-1746186). The computational resources were provided by the Minnesota Supercomputing Institute (MSI) at the University of Minnesota.

REFERENCES

- (1) Willeit, M.; Ganopolski, A.; Calov, R.; Brovkin, V. Mid-Pleistocene transition in glacial cycles explained by declining CO2 and regolith removal. *Sci. Adv.* **2019**, *5*, eaav7337.
- (2) Tollefson, J. How hot will Earth get by 2100? *Nature* **2020**, *580*, 443–445.
- (3) Pennisi, E. Carbon dioxide increase may promote 'insect apocalypse'. *Science* **2020**, *368*, 459–459.
- (4) Karnauskas, K. B.; Miller, S. L.; Schapiro, A. C. Fossil Fuel Combustion Is Driving Indoor CO₂ Toward Levels Harmful to Human Cognition. *GeoHealth* **2020**, *4*, e2019GH000237.
- (5) Jiang, M.; Medlyn, B. E.; Drake, J. E.; Duursma, R. A.; Anderson, I. C.; Barton, C. V. M.; Boer, M. M.; Carrillo, Y.; Castaneda-Gomez, L.; Collins, L.; Crous, K. Y.; De Kauwe, M. G.; Dos Santos, B. M.; Emmerson, K. M.; Facey, S. L.; Gherlenda, A. N.; Gimeno, T. E.; Hasegawa, S.; Johnson, S. N.; Kannaste, A.; Macdonald, C. A.; Mahmud, K.; Moore, B. D.; Nazaries, L.; Neilson, E. H. J.; Nielsen, U. N.; Niinemets, U.; Noh, N. J.; Ochoa-Hueso, R.; Pathare, V. S.; Pendall, E.; Pihlblad, J.; Pineiro, J.; Powell, J. R.; Power, S. A.; Reich, P. B.; Renchon, A. A.; Riegler, M.; Rinnan, R.; Rymer, P. D.; Salomon, R. L.; Singh, B. K.; Smith, B.; Tjoelker, M. G.; Walker, J. K. M.; Wujeska-Klause, A.; Yang, J.; Zaehle, S.; Ellsworth, D. S. The fate of carbon in a mature forest under carbon dioxide enrichment. *Nature* 2020, 580, 227–231.
- (6) van Leeuwen, P. W. N. M.; Freixa, Z. Carbon Monoxide as a Chemical Feedstock: Carbonylation Catalysis. In *Activation of Small Molecules*; Wiley-Blackwell: 2006; pp 319–356, DOI: 10.1002/9783527609352.ch9.
- (7) Can, M.; Armstrong, F. A.; Ragsdale, S. W. Structure, Function, and Mechanism of the Nickel Metalloenzymes, CO Dehydrogenase, and Acetyl-CoA Synthase. *Chem. Rev.* **2014**, *114*, 4149–4174.
- (8) Shin, W.; Lee, S. H.; Shin, J. W.; Lee, S. P.; Kim, Y. Highly selective electrocatalytic conversion of CO_2 to CO at -0.57 V (NHE) by carbon monoxide dehydrogenase from Moorella thermoacetica. *J. Am. Chem. Soc.* **2003**, 125, 14688–9.
- (9) Dobbek, H.; Svetlitchnyi, V.; Gremer, L.; Huber, R.; Meyer, O. Crystal structure of a carbon monoxide dehydrogenase reveals a [Ni-4Fe-5S] cluster. *Science* **2001**, 293, 1281–5.
- (10) Drennan, C. L.; Heo, J.; Sintchak, M. D.; Schreiter, E.; Ludden, P. W. Life on carbon monoxide: X-ray structure of Rhodospirillum rubrum Ni-Fe-S carbon monoxide dehydrogenase. *Proc. Natl. Acad. Sci. U. S. A.* **2001**, *98*, 11973—8.
- (11) Jeoung, J. H.; Dobbek, H. Carbon dioxide activation at the Ni,Fe-cluster of anaerobic carbon monoxide dehydrogenase. *Science* **2007**, *318*, 1461–4.
- (12) Fesseler, J.; Jeoung, J.-H.; Dobbek, H. How the [NiFe₄S₄] Cluster of CO Dehydrogenase Activates CO₂ and NCO⁻. *Angew. Chem., Int. Ed.* **2015**, *54*, 8560–8564.
- (13) Gong, W.; Hao, B.; Wei, Z.; Ferguson, D. J., Jr.; Tallant, T.; Krzycki, J. A.; Chan, M. K. Structure of the $\alpha_2 \varepsilon_2$ Ni-dependent CO dehydrogenase component of the Methanosarcina barkeri acetyl-CoA

- decarbonylase/synthase complex. Proc. Natl. Acad. Sci. U. S. A. 2008, 105, 9558-63.
- (14) Kung, Y.; Doukov, T. I.; Seravalli, J.; Ragsdale, S. W.; Drennan, C. L. Crystallographic snapshots of cyanide- and water-bound C-clusters from bifunctional carbon monoxide dehydrogenase/acetyl-CoA synthase. *Biochemistry* **2009**, *48*, 7432–40.
- (15) Kung, Y.; Drennan, C. L. A role for nickel-iron cofactors in biological carbon monoxide and carbon dioxide utilization. *Curr. Opin. Chem. Biol.* **2011**, *15*, 276–83.
- (16) Osterloh, F.; Saak, W.; Pohl, S. Unidentate and Bidentate Binding of Nickel(II) Complexes to an Fe₄S₄ Cluster via Bridging Thiolates: Synthesis, Crystal Structures, and Electrochemical Properties of Model Compounds for the Active Sites of Nickel Containing CO Dehydrogenase/Acetyl-CoA Synthase. *J. Am. Chem. Soc.* 1997, 119, 5648–5656.
- (17) Majumdar, A. Bioinorganic modeling chemistry of carbon monoxide dehydrogenases: description of model complexes, current status and possible future scopes. *Dalton Trans.* **2014**, *43*, 12135–45.
- (18) Yoo, C.; Kim, Y.-E.; Lee, Y. Selective Transformation of CO₂ to CO at a Single Nickel Center. *Acc. Chem. Res.* **2018**, *51*, 1144–1152.
- (19) Huang, D.; Holm, R. H. Reactions of the terminal Ni(II)-OH group in substitution and electrophilic reactions with carbon dioxide and other substrates: structural definition of binding modes in an intramolecular Ni(II)···Fe(II) bridged site. *J. Am. Chem. Soc.* **2010**, 132, 4693–701.
- (20) Gamba, I. Biomimetic Approach to CO₂ Reduction. *Bioinorg. Chem. Appl.* **2018**, 2018, 2379141.
- (21) Yoo, C.; Lee, Y. Carbon dioxide binding at a Ni/Fe center: synthesis and characterization of Ni(η_1 -CO2- κ C) and Ni- μ -CO2- κ C: κ_2 O,O'-Fe. *Chem. Sci.* **2017**, *8*, 600–605.
- (22) Miller, D. L.; Siedschlag, R. B.; Clouston, L. J.; Young, V. G., Jr.; Chen, Y. S.; Bill, E.; Gagliardi, L.; Lu, C. C. Redox Pairs of Diiron and Iron-Cobalt Complexes with High-Spin Ground States. *Inorg. Chem.* **2016**, *55*, 9725–9735.
- (23) Ramirez, B. L.; Lu, C. C. Rare-Earth Supported Nickel Catalysts for Alkyne Semihydrogenation: Chemo- and Regioselectivity Impacted by the Lewis Acidity and Size of the Support. *J. Am. Chem. Soc.* **2020**, 142, 5396–5407.
- (24) Two molecules of THF are bound to the potassium ion, while a third was found separately in the unit cell of the crystal structure. For a further explanation, see the SI.
- (25) Schwesinger, R.; Link, R.; Wenzl, P.; Kossek, S.; Keller, M. Extremely base-resistant organic phosphazenium cations. *Chem. Eur. J.* **2006**, *12*, 429–37.
- (26) Womble, C. T.; Kang, J.; Hugar, K. M.; Coates, G. W.; Bernhard, S.; Noonan, K. J. T. Rapid Analysis of Tetrakis-(dialkylamino)phosphonium Stability in Alkaline Media. *Organometallics* **2017**, *36*, 4038–4046.
- (27) Carriedo, G. A., Phosphazenes. In *Organophosphorus Chemistry: Volume 37*; The Royal Society of Chemistry: 2008; Vol. 37, pp 262–322, DOI: 10.1039/B704720G.
- (28) Vollmer, M. V.; Cammarota, R. C.; Lu, C. C. Reductive Disproportionation of CO₂ Mediated by Bimetallic Nickelate(-I)/Group 13 Complexes. *Eur. J. Inorg. Chem.* **2019**, 2019, 2140–2145.
- (29) Moore, J. T.; Chatterjee, S.; Tarrago, M.; Clouston, L. J.; Sproules, S.; Bill, E.; Bernales, V.; Gagliardi, L.; Ye, S.; Lancaster, K. M.; Lu, C. C. Enhanced Fe-Centered Redox Flexibility in Fe-Ti Heterobimetallic Complexes. *Inorg. Chem.* **2019**, *58*, 6199–6214.
- (30) Vollmer, M. V.; Xie, J.; Cammarota, R. C.; Young, V. G., Jr.; Bill, E.; Gagliardi, L.; Lu, C. C. Formal Nickelate(-I) Complexes Supported by Group 13 Ions. *Angew. Chem., Int. Ed.* **2018**, *57*, 7815–7819.
- (31) Huber, K. P.; Herzberg, G. Constants of diatomic molecules. In *Molecular Spectra and Molecular Structure: IV. Constants of Diatomic Molecules*; Huber, K. P., Herzberg, G., Eds.; Springer US: Boston, MA, 1979; pp 8–689, DOI: 10.1007/978-1-4757-0961-2_2.
- (32) Tolman, C. A. Phosphorus Ligand Exchange Equilibria on Zerovalent Nickel a Dominant Role for Steric Effects. *J. Am. Chem. Soc.* 1970, 92, 2956.

- (33) Perrin, D. D. Tables. Ionisation Constants of Inorganic Acids and Bases in Aqueous Solution 1982, 1–138.
- (34) Carty, A. J.; Taylor, N. J.; Sappa, E.; Tiripicchio, A.; Tiripicchio Camellini, M. Comparison of the closo trigonal-bipyramidal structures of μ_3 - η^2 -L-acetylene and -acetylide clusters: synthesis of (η_5 - C_5 H $_5$)NiFe $_2$ (CO) $_6$ (μ_3 - η^2 -C \equiv CPr i) and X-ray structures of (η -C $_5$ H $_5$)NiFe 2 (CO) $_5$ (L)(μ_3 - η^2 -C \equiv CR) (R = Pr i , L = CO; R = But, L = PPh $_3$). Organometallics **1991**, 10, 1907–1913.
- (35) Cotton, F. A.; Murillo, C. A.; Walton, R. A. Multiple Bonds Between Metal Atoms; 2005; pp 1-21,.
- (36) Pauling, L. Atomic Radii and Interatomic Distances in Metals. J. Am. Chem. Soc. 1947, 69, 542–553.
- (37) Gütlich, P.; Bill, E.; Trautwein, A. X. Mössbauer Spectroscopy and Transition Metal Chemistry; 2011; DOI: 10.1007/978-3-540-88428-6.
- (38) Amara, P.; Mouesca, J.-M.; Volbeda, A.; Fontecilla-Camps, J. C. Carbon Monoxide Dehydrogenase Reaction Mechanism: A Likely Case of Abnormal CO₂ Insertion to a Ni–H– Bond. *Inorg. Chem.* **2011**, *50*, 1868–1878.
- (39) Mørup, S. Magnetic Relaxation Phenomena. In Mössbauer Spectroscopy and Transition Metal Chemistry; Gütlich, P., Eckhard, B., Trautwein, A. X., Eds.; Springer Verlag: Berlin, 2011; pp 201–234, DOI: 10.1007/978-3-540-88428-6 6.
- (40) See the SI for derivation.
- (41) von Grotthuss, E.; Prey, S. E.; Bolte, M.; Lerner, H. W.; Wagner, M. Selective CO₂ Splitting by Doubly Reduced Aryl Boranes to Give CO and [CO₃]2–. *Angew. Chem., Int. Ed.* **2018**, *57*, 16491–16495.
- (42) von Grotthuss, E.; Prey, S. E.; Bolte, M.; Lerner, H. W.; Wagner, M. Dual Role of Doubly Reduced Arylboranes as Dihydrogen- and Hydride-Transfer Catalysts. *J. Am. Chem. Soc.* **2019**, *141*, 6082–6091.
- (43) Jurd, P. M.; Li, H. L.; Bhadbhade, M.; Field, L. D. Fe(0)-Mediated Reductive Disproportionation of CO₂. *Organometallics* **2020**, 39, 2011.
- (44) Nichols, A. W.; Chatterjee, S.; Sabat, M.; Machan, C. W. Electrocatalytic Reduction of CO2 to Formate by an Iron Schiff Base Complex. *Inorg. Chem.* **2018**, *57*, 2111–2121.
- (45) Costentin, C.; Drouet, S.; Robert, M.; Saveant, J. M. A local proton source enhances CO₂ electroreduction to CO by a molecular Fe catalyst. *Science* **2012**, *338*, 90–4.
- (46) Ostericher, A. L.; Porter, T. M.; Reineke, M. H.; Kubiak, C. P. Thermodynamic targeting of electrocatalytic ${\rm CO_2}$ reduction: advantages, limitations, and insights for catalyst design. *Dalton Trans.* **2019**, 48, 15841–15848.
- (47) Inman, C. J.; Frey, A. S. P.; Kilpatrick, A. F. R.; Cloke, F. G. N.; Roe, S. M. Carbon Dioxide Activation by a Uranium(III) Complex Derived from a Chelating Bis(aryloxide) Ligand. *Organometallics* **2017**, *36*, 4539–4545.
- (48) Lacy, D. C.; McCrory, C. C.; Peters, J. C. Studies of cobalt-mediated electrocatalytic CO₂ reduction using a redox-active ligand. *Inorg. Chem.* **2014**, 53, 4980–8.
- (49) Sampson, M. D.; Kubiak, C. P. Manganese Electrocatalysts with Bulky Bipyridine Ligands: Utilizing Lewis Acids To Promote Carbon Dioxide Reduction at Low Overpotentials. *J. Am. Chem. Soc.* **2016**, *138*, 1386–93.
- (50) Summerscales, O. T.; Frey, A. S.; Cloke, F. G.; Hitchcock, P. B. Reductive disproportionation of carbon dioxide to carbonate and squarate products using a mixed-sandwich U(III) complex. *Chem. Commun.* **2008**, 198–200.
- (51) Lalrempuia, R.; Stasch, A.; Jones, C. The reductive disproportionation of CO₂ using a magnesium(I) complex: analogies with low valent f-block chemistry. *Chem. Sci.* **2013**, *4*, 4383.
- (52) Mokhtarzadeh, C. C.; Moore, C. E.; Rheingold, A. L.; Figueroa, J. S. Terminal Iron Carbyne Complexes Derived from Arrested CO₂ Reductive Disproportionation. *Angew. Chem., Int. Ed.* **2017**, 56, 10894–10899.
- (53) Xémard, M.; Goudy, V.; Braun, A.; Tricoire, M.; Cordier, M.; Ricard, L.; Castro, L.; Louyriac, E.; Kefalidis, C. E.; Clavaguéra, C.;

- Maron, L.; Nocton, G. Reductive Disproportionation of CO₂ with Bulky Divalent Samarium Complexes. *Organometallics* **2017**, *36*, 4660–4668.
- (54) We posit that the presumed [A]**2-CO**₂ (A = [P₁] or [K(B-15-C-6)₂]) species is not a bridging CO_2 adduct or a bridging CO_3^{2-} based on the steric considerations of ligand and the lack of lability of the carbonyl ligand, respectively.
- (55) Pierloot, K. Transition metals compounds: Outstanding challenges for multiconfigurational methods. *Int. J. Quantum Chem.* **2011**, *111*, 3291–3301.
- (56) Dobbek, H., Mechanism of Ni,Fe-Containing Carbon Monoxide Dehydrogenases. In *Metallocofactors that Activate Small Molecules: With Focus on Bioinorganic Chemistry*; Ribbe, M. W., Ed.; Springer International Publishing: Cham, 2019; pp 153–166, DOI: 10.1007/430 2018 27.
- (57) Jeoung, J.-H.; Dobbek, H. Carbon Dioxide Activation at the Ni,Fe-Cluster of Anaerobic Carbon Monoxide Dehydrogenase. *Science* **2007**, *318*, 1461.
- (58) (a) Lindahl, P. A. Metal—metal bonds in biology. *J. Inorg. Biochem.* **2012**, *106*, 172–178. (b) Wittenborn, E. C.; Merrouch, M.; Ueda, C.; Fradale, L.; Leger, C.; Fourmond, V.; Pandelia, M. E.; Dementin, S.; Drennan, C. L. Redox-dependent rearrangements of the NiFeS cluster of carbon monoxide dehydrogenase. *eLife* **2018**, *7*, e39451.
- (59) Murphy, B. J.; Hidalgo, R.; Roessler, M. M.; Evans, R. M.; Ash, P. A.; Myers, W. K.; Vincent, K. A.; Armstrong, F. A. Discovery of Dark pH-Dependent H* Migration in a [NiFe]-Hydrogenase and Its Mechanistic Relevance: Mobilizing the Hydrido Ligand of the Ni-C Intermediate. *J. Am. Chem. Soc.* 2015, 137, 8484–8489.
- (60) Kampa, M.; Pandelia, M. E.; Lubitz, W.; van Gastel, M.; Neese, F. A metal-metal bond in the light-induced state of [NiFe] hydrogenases with relevance to hydrogen evolution. *J. Am. Chem. Soc.* 2013, 135, 3915–25.
- (61) Dickie, C. M.; Laughlin, A. L.; Wofford, J. D.; Bhuvanesh, N. S.; Nippe, M. Transition metal redox switches for reversible "on/off" and "slow/fast" single-molecule magnet behaviour in dysprosium and erbium bis-diamidoferrocene complexes. *Chem. Sci.* **2017**, *8*, 8039–8049
- (62) Barta, O.; Gyepes, R.; Cisarova, I.; Alemayehu, A.; Stepnicka, P. Synthesis and study of Fe -> Pd interactions in unsymmetric Pd(II) complexes with phosphinoferrocene guanidine ligands. *Dalton Trans.* **2020**, *49*, 4225–4229.
- (63) Pick, F. S.; Thompson, J. R.; Savard, D. S.; Leznoff, D. B.; Fryzuk, M. D. Synthesis of Iron and Cobalt Complexes of a Ferrocene-Linked Diphosphinoamide Ligand and Characterization of a Weak Iron-Cobalt Interaction. *Inorg. Chem.* **2016**, *55*, 4059–67.
- (64) Huang, W.; Diaconescu, P. L. Reactivity and Properties of Metal Complexes Enabled by Flexible and Redox-Active Ligands with a Ferrocene Backbone. *Inorg. Chem.* **2016**, *55*, 10013–10023.
- (65) Wei, J.; Diaconescu, P. L. Redox-Switchable Ring-Opening Polymerization with Ferrocene Derivatives. *Acc. Chem. Res.* **2019**, *52*, 415–424
- (66) Bergbreiter, D. E.; Killough, J. M. Reactions of Potassium-Graphite. J. Am. Chem. Soc. 1978, 100, 2126-2134.
- (67) Rudd, P. A.; Liu, S.; Gagliardi, L.; Young, V. G., Jr.; Lu, C. C. Metal-alane adducts with zero-valent nickel, cobalt, and iron. *J. Am. Chem. Soc.* **2011**, *133*, 20724–7.
- (68) Angelici, R. J. Synthesis and technique in inorganic chemistry, 2nd ed.; University Science Books: Mill Valley, CA, 1986; p xiv, 237p.
- (69) Bill, E. personal communication.
- (70) Via KBr pellet a species identifiable as 1-CO is observed, as well as two other species at lower frequencies, potentially due to [Li]2-CO interacting with the potassium ions in the sample matrix. See the SI for further details.
- (71) Blessing, R. H. An empirical correction for absorption anisotropy. *Acta Crystallogr., Sect. A: Found. Crystallogr.* **1995**, *51* (Pt 1), 33–38.

- (72) Sheldrick, G. M. SHELXT integrated space-group and crystal-structure determination. *Acta Crystallogr., Sect. A: Found. Adv.* **2015**, 71, 3–8.
- (73) Sheldrick, G. M. Crystal structure refinement with SHELXL. Acta Crystallogr., Sect. C: Struct. Chem. 2015, 71, 3–8.
- (74) Hubschle, C. B.; Sheldrick, G. M.; Dittrich, B. ShelXle: a Qt graphical user interface for SHELXL. *J. Appl. Crystallogr.* **2011**, 44, 1281–1284.
- (75) Spek, A. L. Structure validation in chemical crystallography. *Acta Crystallogr., Sect. D: Biol. Crystallogr.* **2009**, *65*, 148–55.
- (76) Aquilante, F.; Autschbach, J.; Carlson, R. K.; Chibotaru, L. F.; Delcey, M. G.; De Vico, L.; Fdez Galvan, I.; Ferre, N.; Frutos, L. M.; Gagliardi, L.; Garavelli, M.; Giussani, A.; Hoyer, C. E.; Li Manni, G.; Lischka, H.; Ma, D.; Malmqvist, P. A.; Muller, T.; Nenov, A.; Olivucci, M.; Pedersen, T. B.; Peng, D.; Plasser, F.; Pritchard, B.; Reiher, M.; Rivalta, I.; Schapiro, I.; Segarra-Marti, J.; Stenrup, M.; Truhlar, D. G.; Ungur, L.; Valentini, A.; Vancoillie, S.; Veryazov, V.; Vysotskiy, V. P.; Weingart, O.; Zapata, F.; Lindh, R. Molcas 8: New capabilities for multiconfigurational quantum chemical calculations across the periodic table. *I. Comput. Chem.* **2016**, *37*, 506–541.
- (77) Roos, B. O.; Taylor, P. R.; Sigbahn, P. E. M. A complete active space SCF method (CASSCF) using a density matrix formulated super-CI approach. *Chem. Phys.* **1980**, *48*, 157–173.
- (78) Malmqvist, P. A.; Rendell, A.; Roos, B. O. The restricted active space self-consistent-field method, implemented with a split graph unitary group approach. *J. Phys. Chem.* **1990**, *94*, 5477–5482.
- (79) Malmqvist, P. A.; Pierloot, K.; Shahi, A. R.; Cramer, C. J.; Gagliardi, L. The restricted active space followed by second-order perturbation theory method: theory and application to the study of CuO2 and Cu2O2 systems. *J. Chem. Phys.* **2008**, *128*, 204109.
- (80) Andersson, K.; Malmqvist, P. A.; Roos, B. O.; Sadlej, A. J.; Wolinski, K. Second-order perturbation theory with a CASSCF reference function. *J. Phys. Chem.* **1990**, *94*, 5483–5488.
- (81) Andersson, K.; Malmqvist, P. Å.; Roos, B. O. Second-order perturbation theory with a complete active space self-consistent field reference function. *J. Chem. Phys.* **1992**, *96*, 1218–1226.
- (82) Sauri, V.; Serrano-Andres, L.; Shahi, A. R.; Gagliardi, L.; Vancoillie, S.; Pierloot, K. Multiconfigurational Second-Order Perturbation Theory Restricted Active Space (RASPT2) Method for Electronic Excited States: A Benchmark Study. *J. Chem. Theory Comput.* 2011, 7, 153–68.
- (83) Roos, B. O.; Veryazov, V.; Widmark, P.-O. Relativistic atomic natural orbital type basis sets for the alkaline and alkaline-earth atoms applied to the ground-state potentials for the corresponding dimers. *Theor. Chem. Acc.* **2004**, *111*, 345–351.
- (84) Aquilante, F.; Pedersen, T. B.; Lindh, R. Low-cost evaluation of the exchange Fock matrix from Cholesky and density fitting representations of the electron repulsion integrals. *J. Chem. Phys.* **2007**, *126*, 194106.
- (85) Reiher, M.; Wolf, A. Exact decoupling of the Dirac Hamiltonian. II. The generalized Douglas-Kroll-Hess transformation up to arbitrary order. *J. Chem. Phys.* **2004**, *121*, 10945–56.
- (86) Hirshfeld, F. L. Bonded-atom fragments for describing molecular charge densities. *Theor. Chim. Acta* 1977, 44, 129–138.
- (87) Lu, T.; Chen, F. Multiwfn: a multifunctional wavefunction analyzer. J. Comput. Chem. 2012, 33, 580–92.